Journal of Alloys and Compounds 489 (2010) 202–210

Contents lists available at ScienceDirect

Journal of Alloys and Compounds

journal homepage: www.elsevier.com/locate/jallcom

Optimization of Co-content in C14 Laves phase multi-component alloys for NiMH battery application

K. Young[a,*], T. Ouchi[a], B. Reichman[a], W. Mays[a], R. Regmi[b], G. Lawes[b], M.A. Fetcenko[a], A. Wu[c]

[a] Energy Conversion Devices Inc./Ovonic Battery Company, 2983 Waterview Drive, Rochester Hills, MI 48309, USA
[b] Department of Physics and Astronomy, Wayne State University, Detroit, MI 48201, USA
[c] Shida Battery Company, 30 Xingye Road, Shishan Industrial Park, Foshan, Guangdong 528225, PR China

ARTICLE INFO

Article history:
Received 29 July 2009
Received in revised form 8 September 2009
Accepted 9 September 2009
Available online 16 September 2009

Keywords:
Hydrogen absorbing materials
Transition metal alloys and compounds
Metal hydride
Electrochemical reactions

ABSTRACT

The structural, electrochemical, and gas phase hydrogen storage properties of predominantly C14 crystalline phase alloys with partial replacement by Co (up to 2.5 at%) are reported. Minor phases, including C15 and cubic TiNi, were found by X-ray diffraction and contributed to the improved hydrogen diffusion through the alloy. The optimal Co-content of between 1.0 and 1.5 at% provides easy activation, high gas phase capacity, and a high discharge capacity. An optimized alloy formula also provided the smallest metallic nickel cluster size embedded in the surface oxide and the largest number of nickel clusters. In sealed cell studies, a Co-content of 1.5% gives the best performance in formation, cycle life, and charge retention, but has worse specific power and low temperature performance than some other compositions. The high-rate dischargeabilities at lower rates were found to be limited by surface reactions, not bulk diffusion.

1. Introduction

Nickel–metal hydride (NiMH) batteries are the contemporary energy storage media of choice for hybrid electrical vehicles due to its proven excellence in both safety and endurance. In order to remain competitive with other emerging battery technologies, the capacity of NiMH batteries must be improved. One approach is to replace the rare earth based AB5 metal hydride (MH) electrodes currently used with a higher energy density transition metal based AB2 material. Therefore, it is essential to fully understand the role of each constituent element in the AB2 alloy. Previously, we have investigated the structural and electrochemical properties of C14 based AB2 materials having various combinations of A site elements (Ti and Zr) [1], and B site elements such as vanadium [2], tin [3], manganese [4], aluminum [5], chromium [6,7], nickel [6], and iron [8]. In this paper, we focus on the effects of Co-substitution on the properties of the C14 based AB2 alloys.

Co was the first element substituted for Ni in $LaNi_5$ to extend its cycle life [9,10]. Studies of the interchange between Ni and Co in La(Ni, Co)$_5$ date back to the early 1970s [11,12]. The general effects of Co-substitution on the physical properties of the AB5 electrode were previously reported as: increasing the unit cell volume [11,13,14] but decreasing the volume expansion during hydriding [15–17], decreasing the plateau pressure [11,18,19] and desorption rate [19], reducing hardness [15,17], increasing the absolute value of heat of formation ($|\Delta H|$) [18], reducing the corrosion rate [16], enhancing [20] or impeding hydrogen diffusivity [13], reducing discharge capacity [21] and high-rate dischargeability (HRD) [13,21,22], prolonging the activation process [23], extending the electrochemical cycle life with [21,24] or without [25] the formation of passive oxide on the surface, and promoting self-discharge [26]. More recently, there have been a number of studies on the effects of Co-substitution in the La–Mg–Ni based AB3 or A2B7 alloy families [27–37]. Co-substitution was found to lead to expanding unit cell volume [29], decreasing volume expansion during hydriding [30], lowering equilibrium pressure [29], decreasing PCT hysteresis [29], and increasing PCT slope [29], similar to the effects found in the AB5 alloys. The effects of Co-substitution on the HRD of A2B7 alloys are still under investigation. Reports of both an initial increase in HRD then decrease [30,32] and an initial decrease of HRD followed by a subsequent increase [34] on substituting with Co has appeared in the literature. Similarly, Co-substitution has been reported to both improve [29,31,35,36,37] and degrade [34] cycle stability.

Co-substitution has also been investigated extensively in AB2 alloys as a path to improving performance for both hydrogen storage and battery applications [38–53]. The earliest studies were done by Shaltiel et al. on $Zr(Co_xM_{1-x})_2$ (M = V, Cr, Mn) alloys, which found that as the Co-ontent increased, the PCT plateau pressure increased and the absolute value of heat of formation ($|\Delta H|$) decreased [38]. Honda et al. substituted Co for Mn in C14 $Zr(Mn_{1-x}Co_x)Al_z$ and found that as the cobalt content increased

* Corresponding author. Tel.: +1 248 293 7000; fax: +1 248 299 4520.
E-mail address: kwoyoung@yahoo.com (K. Young).

0925-8388/$ – see front matter © 2009 Elsevier B.V. All rights reserved.
doi:10.1016/j.jallcom.2009.09.052

the plateau pressure/hydrogen absorption speed increased but the storage capacity decreased [39]. Both C14 [44] and C15 [42] $Zr_{1-x}Ti_x(VNiMnM)_\alpha$ alloys with M = Co, Fe, Mo or Cr were studied by Nakano et al; these studies established correlations between the average atomic radius with $|\Delta H|$ and unit cell volume. Electrodes fabricated with Co substituted C14 $ZrCr_{0.8}NiMm_{0.05}Co_{0.2}$ showed a higher equilibrium pressure and a higher discharge capacity at low temperature (0 °C) [40]. Song et al. reported an increase in capacity by partially replacing Ni with Co in $Zr_{0.5}Ti_{0.5}Mn_{0.4}V_{0.6}Ni_{0.85}Co_{0.15}$ [49]. The cycle durability was enhanced by substituting Co in C15 $Ti_{0.8}Zr_{0.2}(V_{0.3}Ni_{0.6}X_{0.1})_2$ alloys, as reported by Chen et al. [42]. A double C14 phase $Zr(Cr_{0.5}Mo_{0.2}Co_{0.3})_2$ exhibiting two PCT absorption plateaus was reported by Bououdina et al. [43]. Additionally, the same group observed increasing $|\Delta H|$ as the Co-ontent increased in $Zr(V_{0.2}Cr_{0.8-x}Co_x)_2$ alloys [45]. A longer cycle life resulting from a reduced PCT hysteresis was observed by Hagström for $Ti_{0.95}Zr_{0.05}Cr_{1.2}Mn_{0.8-x}Co_x$ alloys [46,47]. Equiaxial grains were found for C15 $Zr(NiVMn)_2Co_{0.1}$ leading to an easy activation and higher capacity at the expense of cycle life [48]. Zhu et al. found that by partially replacing Mn with Co in C14 $Ti_{0.8}Zr_{0.2}V_{1.6}Mn_{0.8-x}Co_xNi_{0.6}$ alloy, the cycle durability and high-rate dischargeability were slightly improved [50]. Co was proven to promote the C15 phase in $Zr(Ni_{0.55}Mn_{0.25}V_{0.2-x}Co_x)_2$ and $Zr(Ni_{0.55}Mn_{0.25-x}V_{0.2}Co_x)_2$ in studies by Zhang et al. [51]. Han et al. claimed that in C14 $Zr_{0.9}Ti_{0.1}V_{0.3}Ni_{1.1}Mn_{0.7}X_{0.1}$ alloys, the electrode cycle durability was improved but the charge retention deteriorated with X = Co [52]. Co was found to promote C14 structure and improve the cycle stability and self-discharge as in $ZrCr_{0.4}V_{0.2}Mn_{0.1}Co_xNi_{1.3-x}$ alloys, as reported by Ji et al. [53]. Our previous study on C14-dominated $Ti_{12}Zr_{21.5}V_{10}(NiCrMnSnCoAl)_{56.5}$ alloys indicates that a higher Co-content increases the plateau pressure and reduces both the gas phase and electrochemical storage capacity [6]. Another report from us on C14-dominated $Ti_{18}Zr_{15.5}V_{14}Ni_{24.2-x}Cr_{10}Mn_{17.5}Sn_{0.3}Co_xAl_{0.5}$ alloys shows the addition of Co is beneficial for reducing PCT hysteresis and improving the cycle life [7].

2. Experimental setup

Ingot samples were prepared either by arc melting in a water-cooled copper hearth or by induction melting with a steel pancake-shape mold in an argon atmosphere. The chemical composition of each sample was determined using a Varian *Liberty* 100 inductively-coupled plasma (ICP) system. A Philips *X'Pert Pro* X-ray diffractometer (XRD) is used to study each alloy's microstructure, and a JOEL-*JSM6320F* SEM with X-ray energy dispersive spectroscopy (EDS) capability is used to study phase distribution and composition. PCT characteristics for each sample were measured using a Suzuki-Shokan multi-channel PCT system. In the PCT analysis, each sample is first activated by a 2-h thermal cycle between 300 °C and room temperature at 25 atm H_2 pressure. Details of both electrode and cell preparations as well as measurement methods have been reported previously [2,3,6,54]. Magnetic susceptibility measurement was performed using a Quantum Design MPMS-5T SQUID magnetometer on samples having masses of 30–35 mg.

3. Results and discussion

3.1. Structural properties

Six alloys, CA01–CA06, were prepared by arc melting with the target compositions listed in Table 1. The control alloy, CA01 containing no Co, is the same alloy used in our previous studies [6]. Co-ontent of alloys CA01–CA06 differ by 0.5 at%, with CA06 having 2.5% Co. The Co-substitution occurs at the expense of Ni. Since Co and Ni have similar atomic radii and electronegativity, the partial replacement of Ni by Co does not change the average atomic radius and electronegativity, as seen in Table 1. The average number of outer shell electrons for the A-atom (n_A) and B-atom (n_B) sites and for the AB2 alloy (e/a value) are listed in Table 1. The threshold e/a value for a transition from the C14 to the C15 structure occurs close to 7.00 [55]. Therefore, this group of alloys is expected to have predominantly C14 crystal structure.

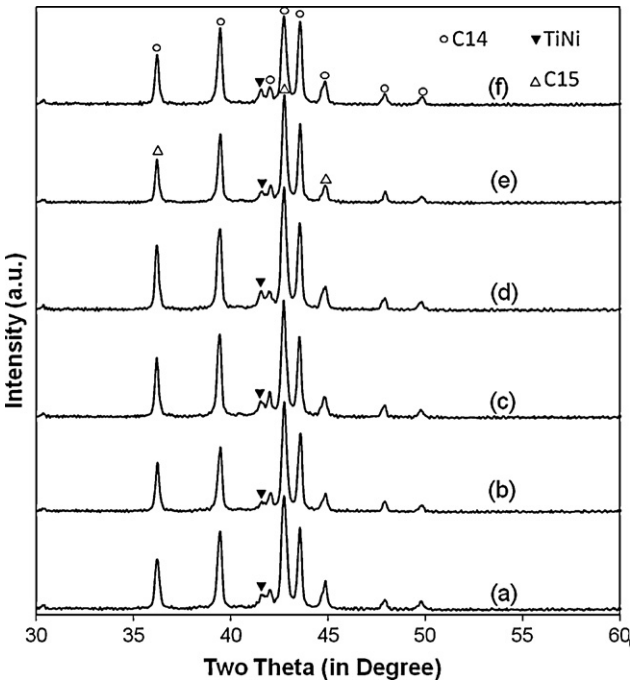

Fig. 1. XRD spectra using Cu Kα as the radiation source for alloys CA01 (a) CA02 (b), CA03 (c), CA04 (d), CA05 (e), and CA06 (f).

XRD patterns for the different samples are shown in Fig. 1 with the results summarized in Table 2. The main phase is C14 having an abundance of about 90%, which increases slightly with increasing Co-ontent. This increase in the C14 relative abundance is consistent with the decreasing e/a values listed in Table 1. Both the a and c lattice constants, together with other XRD parameters such as the a/c ratio, unit cell volume, and full-width at half maximum (FWHM), of the C14 phase are listed in Table 2. These all vary slightly from sample to sample with no clear trends; we attribute these fluctuations to the typical variations expected for arc-melt samples. The second most abundant phase is C15 which accounts for 10% of the total volume. The Bragg peak positions of the C15 reflections overlap with those from the C14 structure. Besides the two Laves phases, there is a cubic phase identified as a δ_1 phase (same as TiNi) in the Ti–Ni–Zr ternary phase diagram, which has a wide solubility of Zr (3–48 at%) with Ni at 48 at% [56]. The lattice constant of this (Ti, Zr)Ni phase (approximately 3.08 Å) is larger than found in the pure TiNi alloy

Table 1
A few important quantities for arc-melt prepared alloys.

Alloy #	Ti	Zr	V	Ni	Cr	Mn	Co	Sn	r_A	r_B	r_A/r_B	r_{av}	X_A	X_B	X_{av}	ΔX	n_A	n_B	e/a
CA01	12	21.5	10	38.1	4.5	13.6	0	0.3	1.550	1.270	1.220	1.364	1.41	1.78	1.65	0.37	4	8.36	6.91
CA02	12	21.5	10	37.6	4.5	13.6	0.5	0.3	1.550	1.270	1.220	1.364	1.41	1.78	1.65	0.37	4	8.36	6.90
CA03	12	21.5	10	37.1	4.5	13.6	1	0.3	1.550	1.270	1.220	1.364	1.41	1.78	1.65	0.37	4	8.35	6.90
CA04	12	21.5	10	36.6	4.5	13.6	1.5	0.3	1.550	1.270	1.220	1.364	1.41	1.78	1.65	0.37	4	8.34	6.89
CA05	12	21.5	10	36.1	4.5	13.6	2	0.3	1.550	1.270	1.220	1.364	1.41	1.78	1.65	0.37	4	8.33	6.89
CA06	12	21.5	10	35.6	4.5	13.6	2.5	0.3	1.550	1.270	1.220	1.364	1.41	1.78	1.65	0.37	4	8.33	6.88

Table 2
Summary of structural, gas phase, and electrochemical properties of alloys prepared by arc-melt.

Alloy number	Crystal structure	Phase abundance	Lattice constant a (in Å)	Lattice constant c (in Å)	Lattice constant ratio (a/c)	Unit cell volume (in Å^3)	Average XRD FWHM	60 °C PCT hysteresis ln(P_a/P_d)	60 °C PCT slope factor	Maximum. PCT capacity (%)	Maximum discharge capacity (mAh/g)	HRD Cap@100/Cap@8 mA/g	Metallic Ni (%)	Ni cluster size in (Å)	Diffusion coefficient, D ($\times 10^{-10}$ cm^2/s)	Exchange current density, I_o (mA/g)
CA01	C14	87%	4.9748	8.1195	0.6127	174.02	0.283	0.17	0.78	1.42	381	94%	0.038	102	26.0	68.5
	TiNi	1.0%	3.080													
CA02	C14	90%	4.9723	8.1105	0.6131	173.65	0.258	0.19	0.79	1.45	382	95%	0.034	115	20.4	63.0
	TiNi	0.7%	3.083													
CA03	C14	87%	4.9771	8.1193	0.6130	174.18	0.255	0.12	0.78	1.62	386	95%	0.041	97	32.4	79.8
	TiNi	2.8%	3.083													
CA04	C14	92%	4.9767	8.1174	0.6131	174.11	0.269	0.12	0.78	1.60	390	95%	0.042	90	17.0	65.3
	TiNi	1.1%	3.085													
CA05	C14	90%	4.9722	8.1199	0.6123	173.85	0.234	0.11	0.79	1.53	379	95%	0.051	100	19.8	69.2
	TiNi	1.8%	3.083													
CA06	C14	94%	4.9736	8.1163	0.6128	173.87	0.268	0.11	0.78	1.44	379	94%	0.046	100	29.9	78.6
	TiNi	2.2%	3.084													

(2.976 Å) due to the partial replacement of Ti by larger Zr atoms. The relative abundance of this phase ranges from approximately 1–3% for the different alloys.

Backscattering electron micrographs from SEM studies of alloys CA01–CA06 are shown in Fig. 2. The bar in the right lower corner of each micrograph indicates length of 20 μm. The numbered areas were studied using EDS analysis and the resulting compositions are listed in Table 3. In general, the C14/C15 (AB2) Laves phases, having a Ti + Zr fraction close to 33–34%, are surrounded by a (Ti, Zr)Ni phase with Ti + Zr fractions between 42% and 44%. The TiNi phase has a brighter contrast due to its higher average atomic mass, owing to the larger Ni-content. ZrO_2 precipitates are observed in each micrograph and exhibit the darkest contrast. EDS could not detect oxygen and the assignment of zirconium oxide instead of zirconium metal is from its atomic mass contrast. Region 6 in CA01 is a mixture of AB2 and ZrO_2. There are three regions belonging to the mixtures of AB2 and TiNi with Ti + Zr fractions between 35% and 38%.

Additionally, the elemental distribution within each alloy was determined using SEM. The Co distribution in the alloys was found to be non-uniform. The atomic percentage of Co in the AB2 phase is more than double that found in the TiNi phase, and is very close to the target design value in Table 1. The V, Cr, Mn distributions are even more inhomogeneous. For example, while V makes up more than 11% of the AB2 phase, the V fraction in the TiNi phase is less than 2.3% of the total. The AB2 Laves phases have higher solubility for Co, V, Cr, and Mn than does the TiNi phase. In the TiNi phase, different contrasts are observed due to the inhomogeneous distribution of Sn. Region 1 in each alloy has a relatively high concentration of Sn, which could be an indication of a possible admixture with a Zr_2Ni_2Sn phase, as reported previously in studies on similar AB2 alloys [8]. The e/a value for each phase is calculated and listed in Table 3. The main AB2 phase has an average e/a value of approximately 6.6–6.8 which indicates that the C14 phase dominates. The C15 phases, having a higher e/a value, could not be resolved with the resolution of the SEM used in this study.

3.2. Gas phase storage properties

The hydrogen gas storage properties of the alloys were studied by PCT. The resulting absorption and desorption isotherms measured at 30 and 60 °C are shown in Fig. 3 and summarized in Table 2. The hysteresis in the PCT isotherm, which is an indicator of particle pulverization [7,57,58], decreases as the Co-content increases. Therefore, Co is found to reduce PCT hysteresis and hence the pulverization, which agrees with our previous study on other C14 alloys [7]. The slope of the PCT isotherm, an indicator for degree of disorder, does not change with an increase in the Co-content, which is a consequence of the similar properties of Co and Ni atoms. The maximum storage capacity determined using the PCT isotherms first increases with increasing Co-ontent, reaches a plateau for the CA03 alloy (Co = 1.0%), and then decreases with a further increase in the Co-content. Desorption pressures at 1% storage capacity at two different temperatures (30 and 60 °C) were used to calculate the change in enthalpy (ΔH) and entropy (ΔS) using the expression:

$$\Delta G = \Delta H - T\Delta S = RT \ln P \quad (1)$$

where R is the ideal gas constant and T is the absolute temperature. The results from these calculations are listed in Table 4. The plateau pressure initially decreases with Co-substitution and then increases as the Co-content is increased. This is in agreement with the generally accepted mechanism where a larger unit cell volume contributes to a more stable hydride with a lower plateau pressure and a higher hydrogen storage capacity [59,60]. Neither the changes in enthalpy nor entropy show any clear trend on Co-substitution.

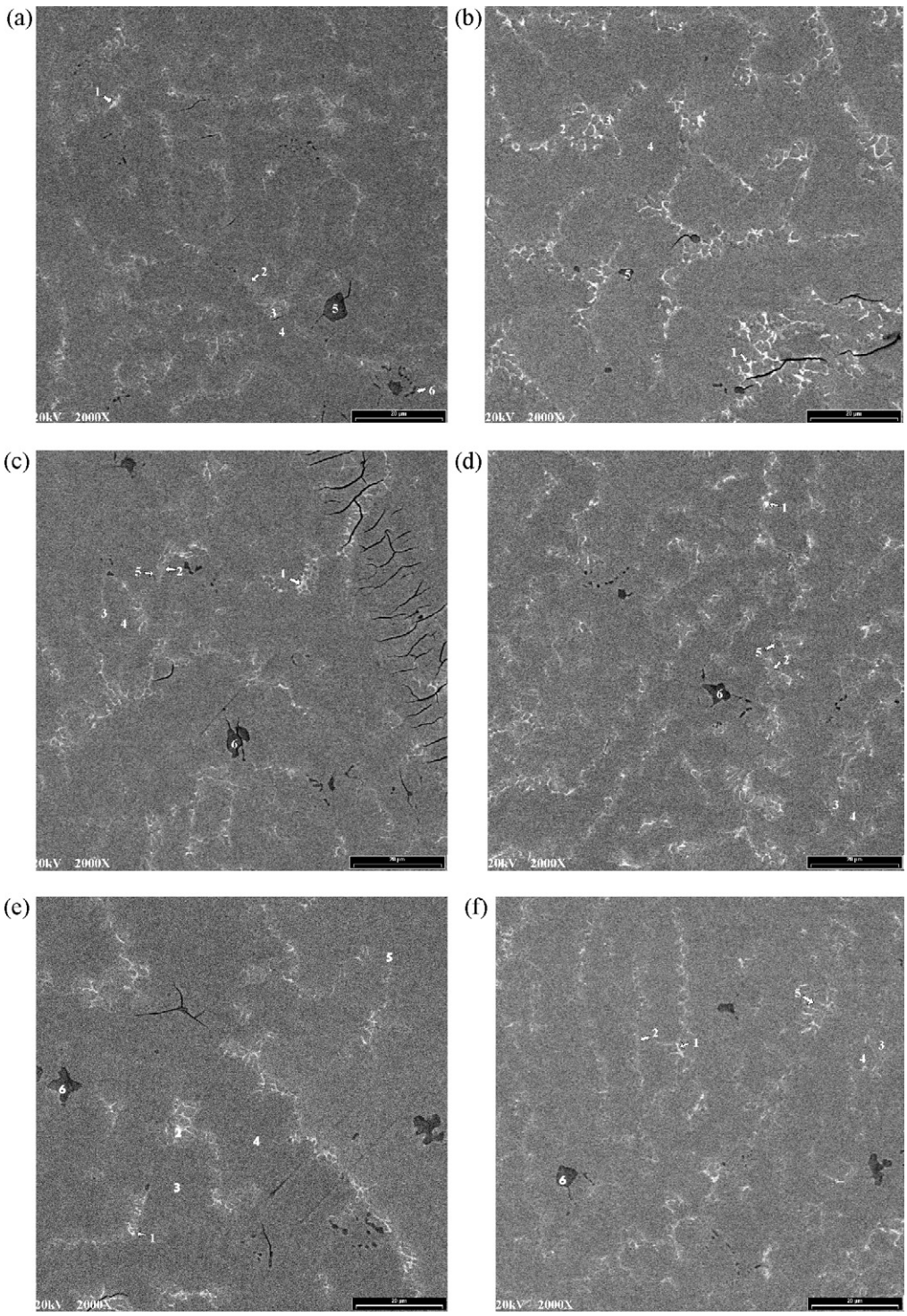

Fig. 2. SEM backscattering electron image micrographs for alloys CA01 (a), CA02 (b), CA03 (c), CA04 (d), CA05 (e), and CA06 (f). The bar on the right lower corner indicates a length of 20 μm. Numbers in each micrograph indicate that EDS analyses were done in these areas and chemical compositions are summarized in Table 3.

This is expected due to the similarity between Ni and Co atoms and also reflects the less uniform structure of the arc-melt prepared samples.

3.3. Electrochemical properties

3.3.1. Small electrode half-cell test

Small electrodes having an area of approximately 1 cm^2 were used to study the activation, capacity, and HRD of these alloys. Capacities from the slowest rate discharge current (8 mA/g) for the first 13 cycles of each alloy are plotted in Fig. 4. The number of formation cycles needed to achieve a high percentage of the maximum capacity decreases from CA01 to CA04 and then increases with increasing Co-content. We therefore conclude that an optimal Co fraction of approximately 1.5% best facilitates the formation process. The maximum capacity for the first 13 cycles of each alloy is listed in Table 2. The capacity follows the same trend as the ease of activation, which increases with the addition of Co, reaches the

Table 3
Chemical composition determined by EDS from regions identified in Fig. 2. The main C14 phase was highlighted by italic style.

Alloy #	Region #	Ti	Zr	V	Ni	Cr	Mn	Co	Sn	Ti + Zr	*e/a*	Phase
CA01	1	15.2	27.3	1.4	45.1	0.1	4.1	0.1	6.7	42.5	6.850	(Ti, Zr)Ni
CA01	2	20.7	21.1	2.2	48.8	0.3	5.2	0.1	1.5	41.8	7.113	(Ti, Zr)Ni
CA01	3	22.2	21.4	1.0	49.6	0.2	3.8	0.1	1.5	43.6	7.101	(Ti, Zr)Ni
CA01	*4*	*11.4*	*22.8*	*11.3*	*36.4*	*2.7*	*14.9*	*0.1*	*0.3*	*34.2*	*6.799*	*C14*
CA01	5	0.3	97.3	0.2	1.3	0.1	0.3	0.2	0.3	97.6	4.101	ZrO_2
CA01	6	9.7	40.4	8.2	29.2	1.7	10.3	0.1	0.4	50.1	6.182	Mixture
CA02	1	15.8	29.0	0.2	44.0	0.1	2.8	0.1	8.0	44.8	6.733	(Ti, Zr)Ni
CA02	2	12.5	22.5	7.4	43.8	1.6	11.5	0.2	0.5	35.0	7.089	Mixture
CA02	3	23.9	19.9	1.0	49.8	0.2	3.9	0.2	1.1	43.8	7.129	(Ti, Zr)Ni
CA02	*4*	*11.1*	*22.9*	*11.4*	*34.9*	*4.0*	*15.1*	*0.4*	*0.2*	*34.0*	*6.761*	*C14*
CA02	5	2.6	87.6	0.8	7.0	0.2	1.2	0.1	0.5	90.2	4.473	ZrO_2
CA03	1	16.5	26.1	1.8	46.4	0.0	4.8	0.1	4.1	42.6	6.943	(Ti, Zr)Ni
CA03	2	20.0	21.8	1.8	49.3	0.1	4.6	0.4	1.9	41.8	7.132	(Ti, Zr)Ni
CA03	3	13.3	23.2	8.9	39.7	0.6	12.7	0.6	0.5	36.5	6.874	mixture
CA03	*4*	*9.6*	*23.9*	*13.7*	*31.2*	*2.9*	*17.3*	*1.0*	*0.2*	*33.5*	*6.628*	*C14*
CA03	5	21.3	21.3	1.9	48.7	0.1	4.7	0.3	1.4	42.6	7.087	(Ti, Zr)Ni
CA03	6	0.9	94.5	0.5	2.6	0.1	0.7	0.2	0.5	95.4	4.194	ZrO_2
CA04	1	16.0	26.8	1.7	45.4	0.1	4.7	0.4	4.9	42.8	6.904	(Ti, Zr)Ni
CA04	2	21.3	22.4	1.3	48.2	0.0	4.2	0.6	1.8	43.7	7.053	(Ti, Zr)Ni
CA04	3	14.3	23.1	8.3	40.1	1.0	11.6	1.0	0.6	37.4	6.907	Mixture
CA04	*4*	*11.3*	*22.7*	*12.0*	*34.5*	*2.3*	*15.5*	*1.5*	*0.2*	*34.0*	*6.776*	*C14*
CA04	5	21.2	22.6	1.8	47.3	0.1	4.7	0.6	1.6	43.8	7.025	(Ti, Zr)Ni
CA04	6	0.4	95.7	0.5	1.8	0.2	0.9	0.2	0.3	96.1	4.154	ZrO_2
CA05	1	20.6	23.1	1.2	47.2	0.0	3.8	0.9	3.2	43.7	7.003	(Ti, Zr)Ni
CA05	2	22.0	20.0	2.0	48.4	0.3	5.1	1.0	1.1	42.0	7.129	(Ti, Zr)Ni
CA05	3	*11.0*	*22.4*	*11.8*	*34.0*	*3.1*	*15.4*	*2.0*	*0.2*	*33.4*	*6.778*	*C14*
CA05	4	*10.2*	*23.8*	*12.7*	*31.4*	*3.8*	*16.1*	*1.8*	*0.2*	*34.0*	*6.660*	*C14*
CA05	5	22.5	20.1	1.7	48.7	0.1	4.8	0.9	1.1	42.6	7.126	(Ti, Zr)Ni
CA05	6	0.4	96.5	0.4	1.6	0.2	0.3	0.2	0.4	96.9	4.123	ZrO_2
CA06	1	19.6	25.2	1.0	45.3	0.0	3.6	1.0	4.1	44.8	6.878	(Ti, Zr)Ni
CA06	2	21.5	20.7	2.3	47.3	0.2	5.4	1.4	1.1	42.2	7.093	(Ti, Zr)Ni
CA06	*3*	*11.3*	*22.3*	*11.8*	*34.0*	*2.9*	*14.9*	*2.4*	*0.3*	*33.6*	*6.779*	*C14*
CA06	*4*	*11.0*	*22.7*	*12.2*	*32.5*	*3.1*	*15.6*	*2.5*	*0.2*	*33.7*	*6.719*	*C14*
CA06	5	22.3	20.8	1.8	47.6	0.2	4.8	1.4	1.1	43.1	7.092	(Ti, Zr)Ni
CA06	6	0.2	97.3	0.3	1.3	0.1	0.3	0.1	0.4	97.5	4.097	ZrO_2

maximum at 390 mAh/g for sample CA04 having a Co fraction of 1.5%, and then decreases as the Co-ontent is increased. The half-cell HRD was determined by taking the ratio between the discharge capacities at 100 and 8 mA/g. The results are plotted in Fig. 5. The 100 mA/g current density was limited by our electrode configuration, which is a dry compaction electrode without any metallic binding. Higher current will cause the electrode to disintegration early in the cycle life. From our previous experience, the flooded half-cell HRD data correlates well with a three times higher current density in a semi-starved condition as in a real NiMH battery. By comparing Figs. 4 and 5, we find it takes more cycles for the HRD to reach its target value than required by the capacity. The HRD values at the 10th cycle are listed in Table 2 and the values fall within a 1% deviation. The individual discharge capacities at three different discharge currents from the 10th cycle are plotted against the atomic percentage of Co in the alloys in Fig. 6. All three capacities increase on Co-substitution and reach a maximum at CA04 (Co = 1.5%).

3.3.2. KOH etching experiment

In order to study the reaction between surface oxide and KOH electrolyte, we conducted an etching experiment by putting 1 g of −200 mesh powder (below 75 μm) in a 7 ml 30% KOH solution in a glass vial at 100 °C for 4 h. Additional 30% KOH solution was placed outside the vial to compensate for liquid lost to evaporation. The concentrations of metal components in the solutes at the end of this treatment were studied by ICP analysis and the results are listed in Table 5. The majority of the solutes are $HZrO_3^-$ and VO_4^{3-} having higher solubility in strong alkaline solutions than the other constituents according to Pourbaix diagrams [61]. The measured concentrations of $ZrHO_3^-$ are much lower than the solubility limits calculated from the equilibrium constants of the equation.

$$ZrO_2(\text{anhydrous}) + H_2O \rightleftarrows ZrHO_3^- + H^+ \quad \text{and} \quad \log([ZrHO_3^-]) = -12.25 + pH \tag{2}$$

The pH value for the 30% KOH solution is −14.84 [62]. The concentration of VO_4^{3-} is also less than the concentration limit given in Ref. [61]. The Al content measured in ICP analysis was leached from the glassware during the hot alkaline bath. The Co contribution is almost undetectable except for the solute from alloys having a higher Co-content (CA05 and CA06). The leaching of Co from this series of alloys is less severe than what is observed in the AB5 compounds [26]. The total solute concentration increases as Co is added to the alloy, reaches maximum for sample CA04 then decreases with increasing Co fraction as plotted in Fig. 7. Therefore, an adequate amount of Co (around 1.5%) is beneficial to the initial formation of the alloy.

As previously reported, clusters of metallic nickel are embedded in the surface oxide of the metal hydride battery electrode [63,64]. These nanoparticles act as a catalyst for surface reactions and are crucial for the high rate and low temperature performance of the battery. The magnetic susceptibility of these metallic nickel clusters is several orders of magnitude larger than from nickel in the alloy due to the availability of unpaired electrons [65], so the amount of metallic nickel on the surface can be estimated from these magnetization measurements. Room temperature magnetization curves as a function of applied magnetic field for each etched powder sample are plotted in Fig. 8. These curves can be fit to the Langevin function

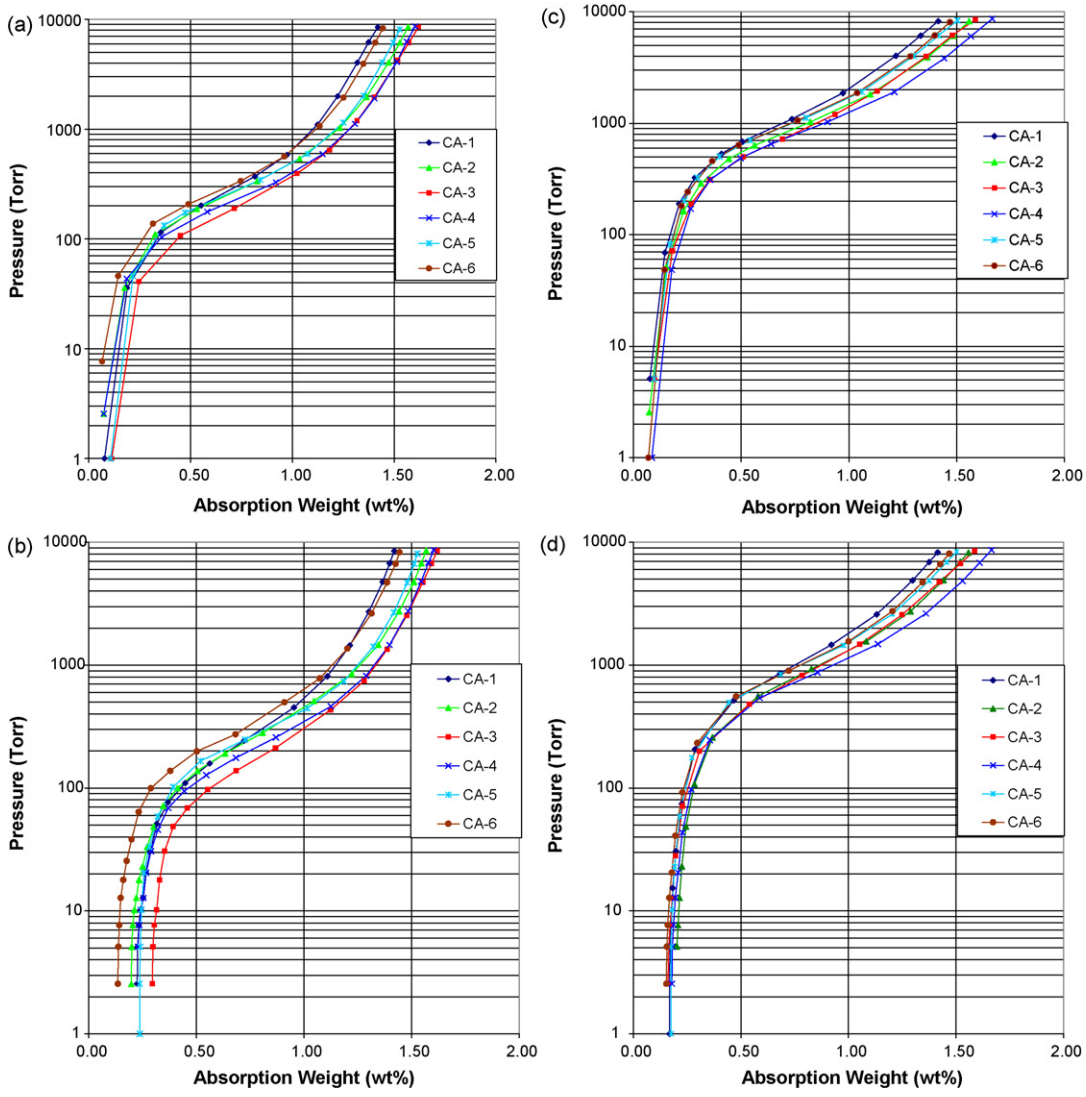

Fig. 3. PCT 30 °C absorption (a), 30 °C desorption (b), 60 °C absorption (c), 60 °C desorption (d) isotherms for alloys CA01 to CA06.

[65]

$$M(H) - \chi_B H = M_S \left\{ \coth\left(\frac{\mu H}{kT}\right) - \frac{kT}{\mu H} \right\} \quad (3)$$

where χ_B is the intrinsic paramagnetic susceptibility, M_S is the saturation magnetization of the metallic Ni, μ is the average magnetic moment of each Ni cluster, k is the Boltzmann constant, and T is the absolute temperature. The content of metallic nickel was calculated from the ratio of estimated M_S for the Ni clusters and known magnetic susceptibility of pure nickel metal, while the size of metallic nickel was estimated from μ using the moment per metallic Ni ($0.6\mu_B$). Both values for each alloy are listed in Table 2 and plotted in Fig. 7. The content of metallic nickel increases while the cluster size decrease as Co is substituted into the alloy. The size of nickel cluster is inversely proportional to the total solute concentration. As more Zr and V leach out from the alloy surface, the residual nickel clusters become smaller. The total number of nickel clusters, which can be obtained from the ratio of metallic nickel percentage

Table 4
Calculation of thermodynamic quantities.

Alloy #	Des. press at 1% and 30 °C (in Torr)	Des. press at 1% and 60 °C (in Torr)	ΔH in (kJ/mol)	ΔS in (J/kmol)
CA01	559	1885	−34.0	−109.6
CA02	466	1352	−29.8	−94.2
CA03	325	1349	−39.8	−124.3
CA04	361	1184	−33.2	−103.4
CA05	433	1564	−35.9	−113.8
CA06	653	1558	−24.3	−79.0

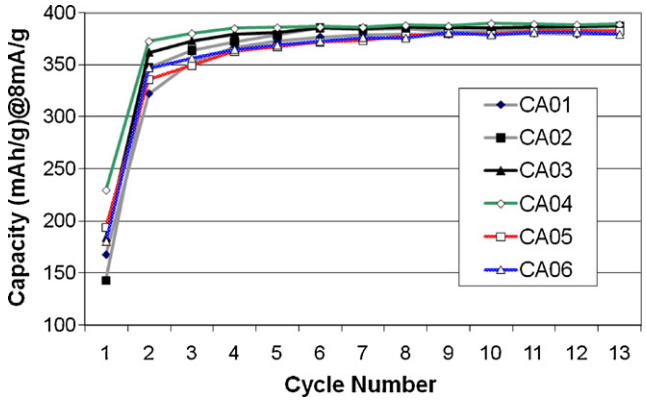

Fig. 4. Evolution of full discharge capacity at a rate of 8 mA/g as a function of cycle number for alloys CA01–CA06.

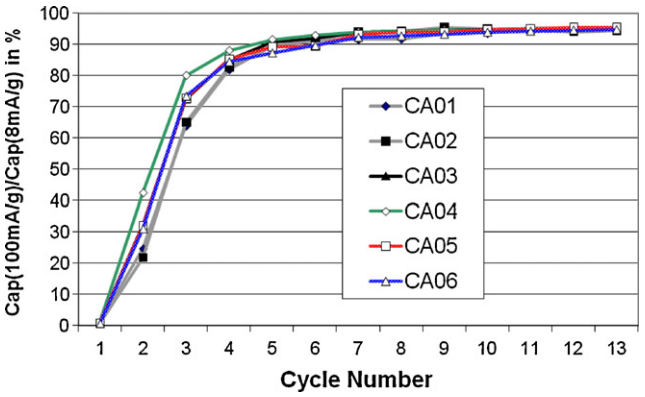

Fig. 5. Evolution of ratio of capacities between 100 mA/g and 8 mA/g rates as a function of cycle number for alloys CA01 to CA06.

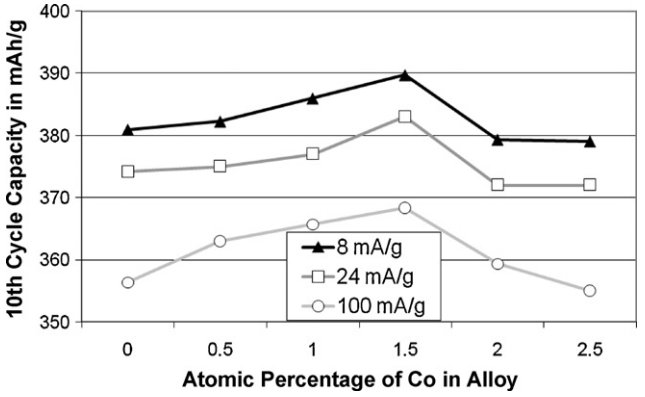

Fig. 6. Discharge capacities at cycle 10 with three rates (8, 24, 100 mA/g) as a function of atomic percentage of Co in alloy.

and the cube of cluster size, follows exactly the trend of total solute concentration in the remaining KOH solution. It first increases on Co-substitution to a maximum value for the CA04 alloy (Co = 1.5%) and then decreases as further Co is added. The trend for total surface area of nickel clusters, which is proportional to the ratio of metallic nickel percentage and the cluster size, is similar to the metallic nickel percentage with a maximum for the CA05 sample (Co = 2.0%).

3.3.3. Measurement of bulk diffusion

The bulk hydrogen diffusion was studied electrochemically for the various alloys using a potentiostatic discharge method described previously [54]. The diffusion coefficient was calculated from the current response plotted on a semi-logarithmic scale vs. time at longer times, where the transport property is dominated by diffusion (time > 2000s). The results are listed in Table 2. Results are plotted together with the C15 and TiNi phase abundances in Fig. 9. It is interesting to note that, although there is no clear trend in the diffusion coefficient as the Co-content increases, the diffusion coefficient is almost linearly dependent on the TiNi phase abundance. This suggests that the bulk diffusion of hydrogen is enhanced

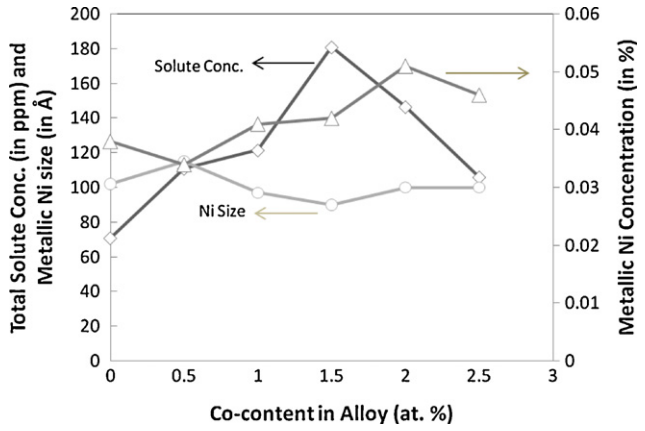

Fig. 7. The total solute concentration, average size and the concentration of metallic nickel cluster as functions of atomic percentage of Co in alloy.

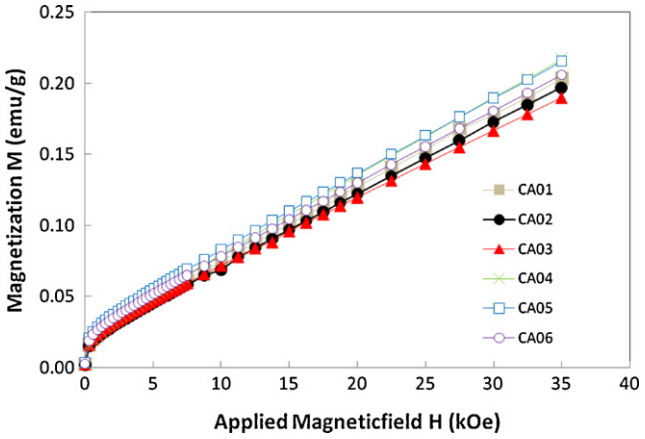

Fig. 8. Room temperature magnetization curves for alloys CA01–CA06.

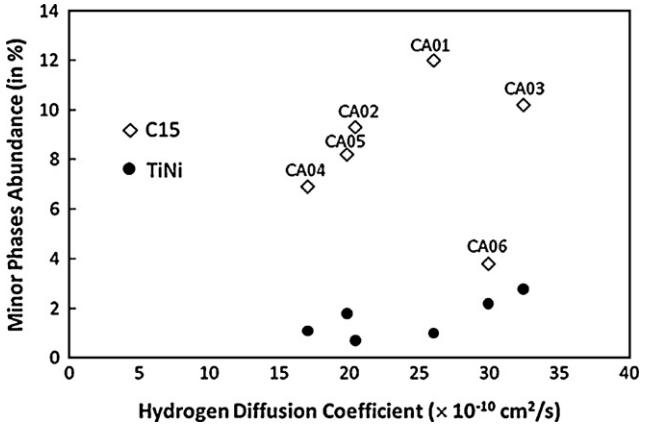

Fig. 9. Graph of the phase abundances of C15 and TiNi vs. hydrogen diffusion coefficient.

Table 5
ICP analysis of solutes in KOH solution after etching 4 h at 100 °C (all numbers are in ppm).

	Al	Co	Cr	Mn	Ni	Sn	Ti	V	Zr	Total solute
CA01	1.6	N.D.	N.D.	1.7	N.D.	N.D.	0.1	49.2	18.3	70.9
CA02	1.5	N.D.	N.D.	4.7	N.D.	5.3	0.7	53.5	44.7	110.4
CA03	2.0	N.D.	N.D.	2.6	N.D.	N.D.	0.9	61.1	53.9	120.6
CA04	0.6	N.D.	N.D.	2.9	N.D.	N.D.	2.2	109.6	64.1	179.4
CA05	1.2	0.8	N.D.	4.0	N.D.	6.4	0.8	77.1	54.2	144.6
CA06	2.2	0.8	N.D.	3.2	N.D.	N.D.	0.6	49.1	47.6	103.4

Table 6
Summary of chemical composition (in atomic percentage), gas phase properties (plateau pressure, slope factor, hysteresis, and maximum capacity), results from half-cell measurement (pre-charge, capacities, and high-rate dischargeability) and full cell (cycle life, charge retention, specific power, and low temperature performance) measurement of a series of induction melted alloys.

	Zr (at%)	Ti (at%)	V (at%)	Cr (at%)	Sn (at%)	Ni (at%)	Mn (at%)	Co (at%)	Al (at%)	Plateau (atm)	Slope factor	PCT hysteresis	Maximum capacity (wt.%)	Precharge (mAh/g)	Cap@ C/7 (mAh/g)	Cap@ C/70 (mAh/g)	Ratio	Cycle life	Charge retention (%)	Specific power (W/kg)	Low temperature (%)
B1	18	15.5	14	10	0.3	24.2	17.5	0	0.5	0.25	0.64	0.26	1.86	61	409	435	0.940	120	28	158	22
B2	18	15.5	14	10	0.3	23.7	17.5	0.5	0.5	0.20	0.56	0.24	1.95	52	400	423	0.946	125	22	139	35
B3	18	15.5	14	10	0.3	22.7	17.5	1.5	0.5	0.17	0.49	0.17	1.90	72	387	414	0.934	145	39	113	10
B4	18	15.5	14	10	0.3	21.7	17.5	2.5	0.5	0.18	0.54	0.13	1.91	86	387	413	0.937	165	65	168	17
C1	12	21.5	10	8.5	0.3	40.2	5.6	1.5	0.4	0.89	0.72	0.22	1.55	17	319	327	0.976	955	40	155	85
C2	12	21.5	10	5.5	0.3	40.2	5.1	5.0	0.4	3.16	0.73	0.13	1.29	21	296	301	0.983	790	16	200	93
C3	12	21.5	10	3.5	0.3	40.2	4.1	8.0	0.4	5.50	0.71	0.05	1.16	28	270	275	0.982	510	25	130	86

by the presence of a secondary phase like TiNi. The dependence of hydrogen diffusion on the C15 fraction is less straightforward, as illustrated by CA06 having a low C15 content but a high diffusion coefficient. These samples were prepared by arc-melt in which the sample homogeneity is difficult to control. Although the secondary phase abundances are not directly related to Co-content, they greatly contribute to the bulk transport property through synergetic effects reported previously [66–69].

3.3.4. Measurement of surface exchange current

The exchange current (I_o) provides a measure of the kinetics in the electrochemical hydrogen reaction at the surface of the electrode. These values were calculated from the electrode polarization using a method described previously [54]. The exchange currents were measured at 50% depth-of-discharge for each alloy in this study, with the results shown in Table 2. The variation of the surface exchange current among alloys is small, and is consistent with the similar values for the half-cell HRD reported in Section 3.3.1. At low rate discharge, the discharge resistance is dominated by the surface reaction and thus does not depend significantly on Co-content. However, at high-rate discharge the bulk diffusion will govern HRD measurements.

3.4. Sealed NiMH battery

3.4.1. Partial replacement of nickel by cobalt

The first series of alloys made for sealed cell studies, B1 to B4, were prepared by a conventional induction melting method. The design compositions of these high capacity alloys were selected to balance different aspects of battery performance and are listed in Table 6. The Co-fractions in these samples are similar to those in CA01–CA06. The B-series of alloys has a general formula of $Zr_{18}Ti_{15.5}V_{14}Cr_{10}Sn_{0.3}Mn_{17.5}Al_{0.5}Co_xNi_{24.2-x}$ where $x = 0.0$, 0.5, 1.5 and 2.5 with a partial replacement of Ni by Co. The structural properties of these alloys have been reported previously [7]. The gas phase, half-cell, and full-cell properties are listed in Table 6. It was observed that as the Co-content in the alloy increases from 0.0% to 2.5%, the PCT plateau pressure decreases (more stable hydride), the PCT isotherm slope factor remains roughly constant (degree of disorder unchanged), and the PCT hysteresis decreases (less pulverization during cycling). Sample B2 exhibits the best overall properties for many of the metrics for battery performance. We find that the maximum gas phase storage capacity peaks for sample B2 (Co = 0.5%), both the high-rate and low-rate electrochemical discharge capacities decrease with the highest ratio obtained at B2, both the cycle life achieving 80% of the original capacity and charge retention improve, and B2 shows the best low temperature capacity. The specific power is maximal for sample B4 (Co = 1.5%).

3.4.2. Partial replacement of manganese and chromium by cobalt

In order to study the role of Co at higher substitution levels, a second series of alloys (C1 to C3) was made for sealed cell study using a 2 kg conventional induction melting method. The target compositions of these three high rate and high cycle life alloys are listed in Table 6. The C-series of alloys has a general formula of $Zr_{21.5}Ti_{12}V_{10}Ni_{40.2}Sn_{0.3}Al_{0.4}Co_{1.5+x+y}Mn_{5.6-x}Cr_{8.5-y}$ where $x = 0.0$, 0.5, 1.5 and $y = 0.0$, 3.0, 5.0 with a partial replacement of Mn and Cr by Co. The rate and cycle life improvement of these samples over the B-series alloys was achieved by combining a smaller fraction of V combined with a higher fraction of Ni. Cr is known to extend the cycle life and improve charge retention but hinder the high-rate dischargeability [6]. Mn is known to improve the charge retention and storage capacity while limiting the cycle life [4]. The gas phase, half-cell, and full-cell properties are listed in Table 6. We find that as the Co-content in the alloy increases from 1.5% to 5.0% and 8.0% at the expense of both Cr and Mn, the

PCT plateau increases (less stable hydride due to the reduction in Mn), the slope factor remains unchanged (same degree of disorder), the PCT hysteresis reduces substantially (less pulverization during cycling), the gas phase maximum storage capacity and electrochemical discharge capacities decrease, the ratio between low-rate and high-rate discharge capacities remains the same, pre-charge increases (easy formation), cycle life reduces (less chromium), both specific power and low temperature capacity reaches maximum when charge retention is the worst at C2 (Co = 5.0).

4. Summary

Through the study of three series of Co-substituted alloys (two to partially replace Ni at low levels, and one to replace Cr and Mn at a higher level), we found the improvement of these properties are not monotonic and an optimum range for Co exists in the following areas:

Structure	Higher Co-content decreases the average electron density and contributes to a higher C14 phase abundance.
Gas phase	A range of Co between 1.0 and 1.5 at% corresponds to a more stable hydride with a lower plateau pressure and a higher hydrogen storage capability.
Half-cell	A Co-content of 1.5 at% yields the highest discharge capacity and easiest formation. Coupled with the overall alloy formula, 1.5% Co also provides the largest number and the smallest metallic nickel inclusions in the surface oxide.
Sealed cell	A Co-content at 1.5% gives the best balance among formation, capacity, cycle life, and charge retention. Unfortunately, both the specific power and low temperature performance are reduced. This suggests that an additional modifier, such as Al, may need to be incorporated into the alloy to optimize the design composition.

References

[1] K. Young, M.A. Fetcenko, F. Li, T. Ouchi, J. Alloys Compd. 464 (2008) 238.
[2] K. Young, M.A. Fetcenko, F. Li, T. Ouchi, J. Koch, J. Alloys Compd. 468 (2009) 482.
[3] K. Young, M.A. Fetcenko, T. Ouchi, F. Li, J. Koch, J. Alloys Compd. 469 (2009) 406.
[4] K. Young, T. Ouchi, J. Koch, M.A. Fetcenko, J. Alloys Compd. 477 (2009) 749.
[5] K. Young, T. Ouchi, B. Reichman, M.A. Fetcenko, R. Regmi, G. Lawes, J. Alloys Compd., submitted for publication.
[6] K. Young, T. Ouchi, M.A. Fetcenko, J. Alloys Compd. 476 (2009) 774.
[7] K. Young, T. Ouchi, W. Mays, B. Reichman, M.A. Fetcenko, J. Alloys Compd. 480 (2009) 434.
[8] K. Young, M.A. Fetcenko, J. Koch, K. Morii, T. Shimizu, J. Alloy Compd., doi:10.1016/j.jallcom.2009.07.004, in press.
[9] J.J.G. Willems, Philips J. Res. 39 (Suppl. 1) (1984) 1.
[10] J.J.G. Willems, K.H.J. Buschow, J. Less-Common Met. 129 (1987) 13.
[11] H.H. Van Mal, K.H.J. Buschow, F.A. Kuijpers, J. Less-Common Met. 32 (1973) 289.
[12] R.A. Guidotti, G.B. Atkinson, M.M. Wong, J. Less-Common Met. 52 (1977) 13.
[13] C. Iwakura, K. Fukuda, H. Senoh, H. Inoue, M. Matsuoka, Y. Yamamoto, Electrochim. Acta 43 (1998) 2041.
[14] R. Baddour-Hadjean, H. Mathlouthi, J.P. Pereira-Ramos, J. Lamloumi, M. Latroche, A. Percheron-Guégan, J. Alloys Compd. 356 (2003) 750.
[15] T. Sakai, K. Oguro, H. Miyamura, N. Kuriyama, A. Kato, H. Ishikawa, J. Less-Common Met. 161 (1990) 193.
[16] G.D. Adzic, J.R. Johnsin, S. Mukerjee, J. McBreen, J.J. Reilly, J. Alloys Compd. 253–254 (1997) 579.
[17] D. Chartouni, F. Meli, A. Züttle, K. Gross, L. Schlapbach, J. Alloys Compd. 241 (1996) 160.
[18] Y. Osumi, H. Suzuki, A. Kato, K. Ogoro, M. Nakane, J. Less-Common Met. 74 (1980) 271.
[19] A. Zarynow, A.J. Goudy, R.G. Schweibenz, K.R. Clay, J. Less-Common Met. 172–174 (1991) 1009.
[20] K. Asano, Y. Hashimoto, T. Iida, M. Kondo, Y. Iijima, J. Alloys Compd. 395 (2005) 201.
[21] T. Sakai, T. Hazama, H. Miyamura, A. Kato, H. Ishikawa, J. Less-Common Met. 172–174 (1991) 1175.
[22] J.K. Chang, D.S. Shong, W.T. Tsai, J. Power Sources 103 (2002) 280.
[23] R.C. Ambrosio, E.A. Ticianelli, J. Power Sources 110 (2002) 73.
[24] T. Vogt, J.J. Reilly, J.R. Johnson, G.D. Adzic, J. McBreen, J. Electrochem. Soc. 146 (1999) 15.
[25] F. Meli, L. Schlapbach, J. Less-Common Met. 172–174 (1991) 1252.
[26] H. Teraoka, Presented in Batteries, Nice, France, September 26–28, 2007.
[27] T. Kohno, H. Yoshida, F. Kawashima, T. Inaba, I. Sakai, M. Yamamoto, M. Kanda, J. Alloys Compd. 311 (2000) L5.
[28] H.G. Pan, Y.J. Yue, M.X. Gao, X.F. Wu, N. Chen, Y.Q. Lei, Q.D. Wang, J. Alloys Compd. 397 (2005) 269.
[29] Y. Liu, H. Pan, M. Gao, R. Li, Y. Lei, J. Alloys Compd. 376 (2004) 296.
[30] H.G. Pan, Y.F. Zhu, M.X. Gao, Y.F. Liu, R. Li, Y.Q. Lei, Q.D. Wang, J. Alloys Compd. 370 (2004) 254.
[31] Y. Liu, H. Pan, M. Gao, R. Li, Y. Lei, J. Alloys Compd. 387 (2004) 147.
[32] Y.F. Liu, H.G. Pan, M.X. Gao, Y.Q. Lei, Q.D. Wang, J. Alloys Compd. 403 (2005) 296.
[33] Y.F. Liu, H.G. Pan, Y.J. Yue, X.F. Wu, N. Chen, Y.Q. Lei, J. Alloys Compd. 395 (2005) 291.
[34] F. Zhang, Y. Luo, K. Sun, D. Wang, R. Yan, L. Kang, J. Chen, J. Alloys Compd. 424 (2006) 218.
[35] H. Miao, H. Pan, S. Zhang, N. Chen, R. Li, M. Gao, Int. J. Hydrogen Energy 32 (2007) 3387.
[36] X. Zhao, Y. Zhang, B. Li, H. Ren, X. Dong, X. Wang, J. Alloys Compd. 454 (2008) 437.
[37] Y. Zhang, X. Dong, B. Li, H. Ren, Z. Wu, X. Wang, J. Alloys Compd. 465 (2008) 422.
[38] D. Shaltiel, I. Jacob, D. Davidov, J. Less-Common Met. 53 (1977) 117.
[39] N. Honda, N. Furukawa, S. Fujitani, I. Yonezu, US Patent 4,913,879 (1990).
[40] S. Kim, J. Lee, J. Alloys Compd. 210 (1994) 109.
[41] H. Nakano, S. Wakao, J. Alloy Compd. 231 (1995) 587.
[42] J. Chen, S.X. Dou, H.K. Liu, J. Alloys Compd. 256 (1997) 40.
[43] M. Bououdina, P. de Rango, D. Fruchart, J.L. Soubeyroux, J. Alloys Compd. 253–254 (1997) 221.
[44] H. Nakano, S. Wakao, T. Shimizu, J. Alloy Compd. 253–254 (1997) 609.
[45] M. Bououdina, J.L. Soubeyroux, D. Fruchart, E. Akiba, K. Nomura, J. Alloys Compd. 235 (1996) 83.
[46] M.T. Hagström, S.N. Klyamkin, P.D. Lund, J. Alloys Compd. 293–295 (1999) 67.
[47] M.T. Hagström, S.N. Klyamkin, E.V. Mescheryakova, P.D. Lund, J. Mater. Sci. 35 (2000) 127.
[48] K.Y. Shu, X.G. Yang, S.K. Zhang, G.L. Lü, Y.Q. Lei, Q.D. Wang, J. Alloys Compd. 306 (2000) 122.
[49] M.Y. Song, D. Ahn, I.H. Kwon, S.H. Chough, J. Electrochem. Soc. 148 (2001) A1041.
[50] Y.F. Zhu, H.G. Pan, G.Y. Wang, M.X. Gao, J.X. Ma, C.P. Chen, Q.D. Wang, Int. J. Hydrogen Energy 26 (2001) 807.
[51] W. Zhang, C. Ma, H. Huang, X. Yang, Y. Lei, Q. Wang, Chin. J. Nonferrous Met. 12 (2002) 897.
[52] S. Han, M. Zhao, L. Wu, Y. Zheng, Chem. J. Chin. Univ. 24 (2003) 2256.
[53] S. Ji, S. Li, J. Sun, Chin. J. Rare Met. 28 (2004) 657.
[54] K. Young, T. Ouchi, Y. Liu, B. Reichman, W. Mays, M.A. Fetcenko, J. Alloys Compd. 480 (2009) 521.
[55] O. Bernauer, J. Topler, D. Noreus, R. Hempolmauu, D. Richter, Int. J. Hydrogen Energy 14 (1989) 187.
[56] V.N. Eremenko, E.L. Semenova, Powder Metal. Ceram. 30 (1991) 664.
[57] K. Young, T. Ouchi, M.A. Fetcenko, J. Alloy Compd. 480 (2009) 428.
[58] K. Young, T. Ouchi, M.A. Fetcenko, J. Alloys Compd. 480 (2009) 440.
[59] M.H. Mendelsohn, D.M. Gruen, A.E. Dwight, Nature (London) 269 (1977) 45.
[60] M.H. Mendelsohn, D.M. Gruen, A.E. Dwight, J. Less-Common Met. 63 (1979) 193.
[61] M. Pourbaix, Atlas of Electrochemical Equilibria in Aqueous Solution, 2nd English edition, NACE, Houston, Texas, USA, 1974.
[62] R.C. Weast (Ed.), CRC Handbook of Chemistry and Physics, 60th edition, CRC Press, Inc., Boca Raton, Florida, USA, 1979, p. D-253.
[63] M.A. Fetcenko, S.R. Ovshinsky, K. Young, B. Reichman, C. Fierro, J. Koch, W. Mays, T. Ouchi, B. Sommers, A. Zallen, J. Alloys Compd. 330–332 (2002) 752.
[64] M.A. Fetcenko, S.R. Ovshinsky, B. Reichman, K. Young, C. Fierro, J. Koch, A. Zallen, W. Mays, T. Ouchi, J. Power Sources 165 (2007) 544.
[65] F. Stucki, L. Schlapbach, J. Less-Common Met. 74 (1980) 143.
[66] W.K. Zhang, C.A. Ma, X.G. Yang, Y.Q. Lei, Q.D. Wang, Trans. Nonferrous Met. Chin. 19 (1999) 505.
[67] Q.A. Zhang, Y.Q. Lei, X.G. Yang, Y.L. Du, Q.D. Wang, J. Alloys Compd. 305 (2000) 125.
[68] M. Bououdina, J.L. Soubeyroux, D. Fruchart, J. Alloys Compd. 327 (2001) 185.
[69] A. Visintin, H.A. Peretti, F. Ruiz, H.L. Corso, W.E. Triaca, J. Alloys Compd. 428 (2007) 244.